The Astrophysical Journal, 932:12 (10pp), 2022 June 10 https://doi.org/10.3847/1538-4357/ac6c90

Radio Spectral Energy Distributions for Single Massive Star Winds with Free–Free and Synchrotron Emission

Christiana Erba and Richard Ignace
Department of Physics and Astronomy, East Tennessee State University, Johnson City, TN 37614, USA; christi.erba@gmail.com
Received 2022 February 7; revised 2022 May 1; accepted 2022 May 2; published 2022 June 9

Abstract

The mass-loss rates from single massive stars are high enough to form radio photospheres at large distances from the stellar surface, where the wind is optically thick to (thermal) free–free opacity. Here we calculate the far-infrared, millimeter, and radio band spectral energy distributions (SEDs) that can result from the combination of free–free processes and synchrotron emission, to explore the conditions for nonthermal SEDs. Simplifying assumptions are adopted in terms of scaling relations for the magnetic field strength and the spatial distribution of relativistic electrons. The wind is assumed to be spherically symmetric, and we consider the effect of Razin suppression on the synchrotron emission. Under these conditions, long-wavelength SEDs with synchrotron emission can be either more steep or more shallow than the canonical asymptotic power-law SED from a nonmagnetic wind. When nonthermal emission is present, the resultant SED shape is generally not a power law; however, the variation in the slope can change slowly with wavelength. Consequently, over a limited range of wavelengths, the SED can masquerade as approximately a power law. While most observed nonthermal long-wavelength spectra are associated with binarity, synchrotron emission can have only a mild influence on single-star SEDs, requiring finer levels of wavelength sampling for the detection of the effect.

Unified Astronomy Thesaurus concepts: Non-thermal radiation sources (1119); Early-type stars (430); Stellar magnetic fields (1610); Stellar mass loss (1613); Stellar winds (1636); Radio continuum emission (1340)

1. Introduction

Massive stars are an important part of the story of cosmic evolution (e.g., Bromm & Larson 2004; Heger & Woosley 2010; Madau & Dickinson 2014), due to their luminous but short lifetimes (e.g., Langer 2012), their explosive endings (e.g., Woosley et al. 2002), the extreme remnants that they produce (e.g., Heger et al. 2003), and their strong influence on galactic evolution (e.g., Hopkins et al. 2012). Our developing understanding of massive star evolution is informed by factors such as stellar rotation, magnetism, and mass-loss rates. Ongoing observational and theoretical investigations continue to refine our ability to measure and interpret these properties for massive stars.

Radio studies are a foundational approach for determining the relatively high mass-loss rates ($\dot{M}$) from massive stars, which can be large enough to produce radio photospheres that form in the stellar wind (Panagia & Felli 1975; Wright & Barlow 1975; Abbott et al. 1980, 1981, 1986; Bieging et al. 1989; Leitherer et al. 1995, 1997). The radio flux ($\mathcal{F}_\nu$) is typically attributed to thermal (free–free) emission, and is proportional to both the mass-loss rate of the star and the terminal velocity of the wind (v_∞), via $\mathcal{F}_\nu \propto (\dot{M}/v_\infty)^{4/3}$ (Lamers & Cassinelli 1996). However, additional factors such as globally structured magnetic fields (e.g., Owocki & ud-Doula 2004; Daley-Yates et al. 2019), nonthermal emission from gyrosynchrotron processes (e.g., White 1985; Chen & White 1994; Van Loo et al. 2006), and the existence of structured wind flows ("clumping"; e.g., Blomme & Runacres 1997; Nugis et al. 1998; Fullerton et al. 2006; Puls et al. 2006; Ignace 2016), have presented challenges for how radio measures can be used to infer $\dot{M}$ values. An improved understanding of how these processes affect the shape of the spectral energy distribution (SED), and thus interpretations of the stellar mass-loss rate, is therefore required.

The discussion of nonthermal radio emission from massive stars has often focused on synchrotron emission in massive colliding wind binaries (CWBs; e.g., Williams et al. 1994; Pittard et al. 2006; Falceta-Goncalves & Abraham 2012; Parkin et al. 2014; Benaglia et al. 2015; De Becker et al. 2017). Electrons are accelerated at the shocks formed from the collision of highly supersonic wind flows, and the in situ magnetism where synchrotron emission is generated derives from a stellar magnetic field. A tremendous advantage of a CWB system is the opportunity to observe cyclical variations in the nonthermal spectrum. This variability provides diagnostic leverage to produce globally self-consistent models for the wind properties, shock properties, magnetism, and the physics underlying particle acceleration (e.g., Blomme et al. 2017; De Becker 2018).

Although CWB systems have considerable potential to describe the nonthermal emission from massive star binaries, they cannot be used to fully characterize the nonthermal emission from (purportedly) single early-type stars. In recent years, an increasing number of these have been detected, in no small part due to the successes of the spectropolarimetric surveys that have provided direct measurements of large-scale, nearly dipolar[1] surface magnetic fields in massive stars (e.g., MiMeS, BOB; Alecian et al. 2014; Fossati et al. 2015;

[1] The assumption of a (nearly) dipolar magnetic topology is generally appropriate (e.g., Donati & Landstreet 2009). However, there are some notable exceptions, including τ Sco (HD 149438, B0.2 V; Donati et al. 2006), HD 37776 (B2V; Kochukhov et al. 2011), and α^2 CVn (B9p; Silvester et al. 2014), which have fields with significantly more complex magnetic topologies.

Morel et al. 2015; Wade et al. 2016; Grunhut et al. 2017). The magnetic fields of O- and B-type stars channel the stellar wind into a structurally complex magnetosphere, which can provide the conditions necessary for synchrotron emission (e.g., Trigilio et al. 2004; Leto et al. 2006, 2021; Shultz et al. 2022). Nonthermal radio spectra of single magnetic massive stars have been observed in several instances (e.g., Kurapati et al. 2017; Leto et al. 2017, 2018).

White (1985) published a seminal paper exploring the modeling and application of radio synchrotron emission for massive star winds. The work was later expanded by Chen & White (1991), White & Chen (1992), Chen & White (1994), and White & Chen (1994), both in terms of including additional physical processes (e.g., inverse Compton cooling), and for the consideration of very-high-energy emissions. Two developments emerged from this series. First, it appeared that the majority of sources displaying nonthermal radio emission were in binaries, hence the increased focus on the modeling of CWB systems (e.g., Dougherty et al. 2003; Pittard et al. 2021). Second was the recognition that there are challenges to understanding how relativistic electrons can survive and/or be energized at large radii in the wind (Van Loo et al. 2004, 2005, 2006). While these challenges remain, nonthermal radio emission has been observed in a few nonmagnetic, purportedly single, early-type stars (e.g., Dougherty & Williams 2000). There is thus a need to further develop the theoretical description of how free–free and nonthermal emission jointly affect the SED, in order to provide benchmarks for these data.

In this paper, we present several new models of far-infrared, millimeter, and radio band spectral energy distributions (SEDs) resulting from the combination of thermal (free–free) and nonthermal (synchrotron) emissions. Section 2 develops the model components. In particular, our goal is to examine general trends for single-star winds, and to this end we consider spherical winds and adopt scaling relations for the magnetic field strength and the density of high-energy electrons. Section 3 reports the results of our analysis. Finally, in Section 4, we discuss these results in light of the current data and interpretation of radio SEDs for massive-star winds.

2. Modeling Radio SEDs

2.1. Thermal Free–Free Emission

Our model is based on a smooth, spherically symmetric wind. While it is clear that magnetism can alter the wind density and vector flow from a spherical geometry, a spherical wind is appropriate for a qualitative exploration of how synchrotron emission can influence radio SED shapes. Additionally, unlike numerically intensive MHD simulations and detailed radiative transfer, the semi-analytic approaches afforded by simplifying assumptions (such as a spherical wind density) allow for a rapid exploration of the parameter space.

The emission coefficient for thermal free–free processes, expressed in terms of the power per unit frequency per unit volume per steradian, is written as (e.g., Rybicki & Lightman 1986)

$$j_\nu^{\rm ff} = 5.45 \times 10^{-39}\, Z_{\rm i}^2\, n_{\rm e} n_{\rm i}\, T^{-1/2}\, g_\nu^{\rm ff}\, e^{-h\nu/kT}, \quad (1)$$

where $Z_{\rm i}$ is the root-mean-square charge of the ion, T is the gas temperature, $n_{\rm e}$ and $n_{\rm i}$ are respectively the free electron and ion densities, ν is the observation frequency, and $g_\nu^{\rm ff}$ is the free–free Gaunt factor (e.g., Brussaard & van de Hulst 1962; Hummer 1988). In the exponential, h and k are the usual Planck and Boltzmann constants. The numerical constant has been evaluated in cgs units.

In the Rayleigh–Jeans limit appropriate at long wavelengths where $h\nu \ll kT$, the expression for the emission coefficient becomes

$$j_\nu^{\rm ff} \approx 5.45 \times 10^{-14}\, Z_{\rm i}^2 \left(\frac{n_{\rm e} n_{\rm i}}{10^{26}}\right)\left(\frac{10^4}{T}\right)^{1/2} g_\nu^{\rm ff}, \quad (2)$$

where we have scaled the temperature and ion number densities by fiducial values similar to those found in massive star winds.

The absorption coefficient, written here as the product of the opacity coefficient and the mass density, is given by (e.g., Rybicki & Lightman 1986)

$$(\kappa_\nu\, \rho)^{\rm ff} = 3.7 \times 10^8\, Z_{\rm i}^2\, n_{\rm e} n_{\rm i}\, T^{-1/2}\, \nu^{-3}\, g_\nu^{\rm ff}(1 - e^{-h\nu/kT}), \quad (3)$$

which, in the Rayleigh–Jeans limit, is approximated as

$$(\kappa_\nu\, \rho)^{\rm ff} \approx 0.0020\, Z_{\rm i}^2\, \frac{n_{\rm e} n_{\rm i}}{10^{26}}\left(\frac{10^4}{T}\right)^{3/2} \lambda^2\, g_\nu^{\rm ff}. \quad (4)$$

Note that we now express the absorption coefficient in terms of the observation wavelength λ. The source function for free–free radiation is therefore

$$S_\nu^{\rm ff} = \left(\frac{j_\nu}{\kappa_\nu \rho}\right)^{\rm ff} = B_\nu \approx \frac{2kT}{\lambda^2} = 2.8 \times 10^{-12}\, \lambda^{-2}\left(\frac{T}{10^4}\right). \quad (5)$$

We can estimate the extent of the radial photosphere (Cassinelli & Hartmann 1977), assuming that the wind is optically thick to the free–free opacity (Equation (4)), with the speed $v(r) \approx v_\infty$. The optical depth of a location in the wind is given by the integral of the free–free opacity along the observer's line of sight (LOS),

$$\tau_\nu^{\rm ff} = \int (\kappa_\nu \rho)^{\rm ff}\, dz, \quad (6)$$

where $z = \varpi \cot\theta$, ϖ is the impact parameter for a ray through the wind, and θ gives the angle between the radial direction and the observer's LOS.

We introduce R_ν as the radius at which an optical depth of unity is achieved, defined through

$$\tau_\nu^{\rm ff} = \int_{R_\nu}^{\infty} (\kappa_\nu \rho)^{\rm ff}\, dr = 1. \quad (7)$$

For an isothermal wind with $T = 10^4$ K, setting $Z_{\rm i} = 1$, along with $n_{\rm e} = n_{\rm i}$, the effective radius R_ν, expressed in terms of the stellar radius R_*, is

$$\frac{R_\nu}{R_*} \approx 405\left(\frac{\lambda}{\lambda_0}\right)^{2/3}\left(\frac{n_0}{10^{13}}\right)^{2/3}\left(\frac{R_*}{10^{11}}\right)^{1/3}(g_\nu^{\rm ff})^{1/3}, \quad (8)$$

Here, we scale the wavelength by a fiducial value of $\lambda_0 = 1$ cm, and the stellar radius by 10^{11} cm $\sim 1.5 R_\odot$. The number density

scale constant n_0, where

$$n_0 = \frac{\dot{M}}{4\pi\ \mu_e\ m_H R_*^2\ v_\infty}, \tag{9}$$

is derived from mass continuity (assuming spherical symmetry), where $\dot{M}$ is the mass-loss rate, v_∞ is the terminal velocity of the wind, and μ_e is the mean molecular weight per free electron. With $n_e = n_i$, a wind of entirely ionized hydrogen would have $\mu_e = 1$, whereas a wind of entirely singly ionized helium would have $\mu_e = 4$.

Equation (8) shows that the extent of the radio photosphere increases with wavelength, although the increase is more shallow than that from a linear dependence on λ. The radio photosphere at $\lambda_0 = 1$ cm, assuming $n_0 = 10^{13}\,\mathrm{cm}^{-3}$, is extensive;[2] however, ion abundances, the temperature and ionization state of the gas, and the stellar radius will realistically alter the value of R_ν, even assuming that n_0 does not change. Furthermore, the presence of clumping (structured wind flows believed to result from the intrinsic instabilities associated with the wind-driving physics; see, e.g., Lucy & White 1980; Owocki et al. 1988) in the wind would also extend the radio photosphere (Ignace 2016).

Radio SEDs purely from free–free opacity have been well studied. Wright & Barlow (1975) and Panagia & Felli (1975) derived the canonical SED power-law result, with the radio flux $\mathcal{F}_\nu \propto \nu^{-0.6}$ for a spherical wind, at long ($\sim$1 cm) wavelengths for which the extent of the radio photosphere is much greater than the stellar radius. Schmid-Burgk (1982) found that under the assumption of power-law distributions for the wind density and temperature, axisymmetric winds have SED slopes with the same power-law dependence of the frequency ($\propto\nu^{-0.6}$) as from spherically symmetric winds (although the luminosity level is different from the spherical result). This highlighted the idea that the SED slope is governed by the isophotal growth rate as a function of wavelength. Power-law SEDs result for isophotes whose shapes are invariant with wavelength. Ultimately, the expanding radio photosphere with wavelength provides an opportunity for mapping the wind density and geometry as a function of wavelength. For example, the canonical result of $\mathcal{F}_\nu \propto \nu^{-0.6}$, while not unique, can generally be taken as evidence of a spherically symmetric wind expanding at a constant speed.

Free–free radio SEDs have been evaluated for a variety of additional considerations. A change in the SED power-law slope can result from a change in the geometry of the circumstellar medium. The study of Be stars performed by Klement et al. (2017) provides a useful example. The authors found that disk truncation can lead to an SED slope that steepens toward $\mathcal{F}_\nu \propto \nu^{-2}$, which is suggestive of an as yet undetected binary companion. The influence of clumping for free–free radio SEDs has also been considered (e.g., Abbott et al. 1981; Blomme & Runacres 1997; Ignace et al. 2003; Ignace 2016). Clumping affects the opacity, impacting the location of the effective radius R_ν. Clumping also increases the emissivity, which scales as the square of density. The end result is that mass-loss rates derived from radio luminosities will be overestimated if clumping is not taken into account.

[2] A wind density scale of $n_0 = 10^{13}\,\mathrm{cm}^{-3}$ is applicable to WR stars, which have a very dense wind environment. For OB supergiants, a wind density scale of $n_0 = 10^{10}\,\mathrm{cm}^{-3}$ would be more appropriate. See also Appendix C.

2.2. Synchrotron Emission

For a single electron, the specific luminosity of synchrotron emission is (Rybicki & Lightman 1986; Dougherty et al. 2003)

$$L_\nu = \sqrt{3}\ \frac{q^3\ B \sin\alpha}{m_e\ c^2}\ F(\nu/\nu_c), \tag{10}$$

where B is the magnetic field strength, m_e is the electron mass, q is the electron charge, α is the pitch angle, and $F(x)$ gives the spectral slope as a function of frequency. The quantity ν_c is the cutoff frequency, given by

$$\nu_c = \frac{3\gamma^2\ q\ B \sin\alpha}{4\pi\ m_e\ c}, \tag{11}$$

where γ is the Lorentz factor of the relativistic electrons. For an electron, $\nu_c = 4.2\,\mathrm{MHz}\,\gamma^2 B \sin\ \alpha$, or in terms of wavelength, $\lambda_c = 0.071\ \mathrm{km}(\gamma^2\ B \sin\alpha)^{-1}$.

The synchrotron spectrum can be derived from a power-law distribution of free electrons. At a given location in the wind, the energy distribution of the electron number density can be represented as

$$\frac{dn_\gamma(r, E)}{dE}\,dE = C_E(r) E^{-p(r)}\,dE, \tag{12}$$

where E is the energy, C_E is a scale constant, and p is the power-law exponent for the distribution. This can be recast in terms of the Lorentz factor for the relativistic electrons, with

$$\frac{dn_\gamma(r, \gamma)}{d\gamma}\,d\gamma = C_\gamma(r)\gamma^{-p(r)}\,d\gamma, \tag{13}$$

where C_γ is the corresponding scale constant. Note that with respect to units, $C_\gamma \sim$ number density, but C_E has units of energy that depend on the value of p. The ratio of the scale constants is thus

$$\frac{C_\gamma}{C_E} = (m_e\ c^2)^{1-p}. \tag{14}$$

The value of the scale constants C_γ and C_E can vary with pitch angle (Rybicki & Lightman 1986), but we ignore such pitch-angle effects for this study.

The number density of the relativistic electrons associated with the production of synchrotron emission is then

$$n_\gamma(r) = C_\gamma(r) \int_{\gamma_{min}}^{\gamma_{max}} \gamma^{-p}\,d\gamma. \tag{15}$$

The power-law index p can vary with radius (e.g., Van Loo et al. 2005), but we choose[3] a constant value of $p(r) = p_0 = 2$, which is commonly adopted for strong shocks (see Ellison & Eichler 1985; Eichler & Usov 1993, and sources therein).

If we assume $\gamma_{min} \sim 1$ and $\gamma_{max} \gg 1$ for all locations in the wind, the number density of relativistic electrons becomes

$$n_\gamma(r) \approx C_\gamma(r) \equiv C_* \left(\frac{R_*}{r}\right)^{m+2}, \tag{16}$$

where m is a power-law exponent that is a free parameter of our model. The case of $m = 0$ corresponds to an inverse-square

[3] Other values could certainly be used: Van Loo et al. (2004) suggest a steeper value, with p_0 between 2 and 3. We adopt here the choice of $p_0 = 2$ to facilitate our quantitative examples.

decline of the density of the high-energy elections C_γ, matching the scaling of the gas density with radius in the asymptotic constant expansion portion of the wind.

Simplifying for the specific case of $p_0 = 2$, we find that $C_E = C_\gamma m_e c^2$. Assuming equipartition, the scale constant for the particle distribution is expressed as (Dougherty et al. 2003)

$$C_\gamma = \frac{u_{\rm rel}/m_e\, c^2}{\ln \gamma_{\rm max}} \left(\frac{R_*}{r}\right)^{m+2}, \tag{17}$$

where $u_{\rm rel}$ is the energy density of the relativistic particles, and $\gamma_{\rm max}$ is the largest value of γ achieved by any particle.

The emission coefficient for synchrotron processes, expressed as power per unit frequency per unit volume per steradian, is (Rybicki & Lightman 1986)

$$j_\nu^{\rm s} = \frac{\sqrt{3} q^3 B}{4\pi m_e\, c^2} \frac{C_\gamma}{p+1} \Gamma\left(\frac{p}{4} + \frac{19}{12}\right) \Gamma\left(\frac{p}{4} - \frac{1}{12}\right) \times \left(\frac{2\pi\ m_e\ c\ \nu}{3qB}\right)^{(1-p)/2}, \tag{18}$$

where we choose $\alpha = 90°$ for the pitch angle.

The absorption coefficient for synchrotron processes is given by Rybicki & Lightman (1986)

$$(\kappa_\nu \rho)^{\rm s} = \frac{\sqrt{3} q^3}{8\pi\ m_e} \left(\frac{3q}{2\pi\ m_e^3\ c^5}\right)^{p/2} B^{(p+2)/2}\ \nu^{-(p+4)/2} \times C_E\, \Gamma\left(\frac{p}{4} + \frac{1}{6}\right) \Gamma\left(\frac{p}{4} + \frac{11}{6}\right). \tag{19}$$

The source function for the synchrotron emission is then

$$S_\nu^{\rm s} = \frac{j_\nu^{\rm s}}{(\kappa_\nu \rho)^{\rm s}} \tag{20}$$

$$= \frac{2\, m_e^p\, c^{2p}\, \nu^{5/2}}{c^2} \left(\frac{2\pi\ m_e\ c}{3qB}\right)^{1/2} \frac{C_\gamma}{C_E} \frac{\tilde{\Gamma}(p)}{p+1}, \tag{21}$$

where

$$\tilde{\Gamma}(p) \equiv \frac{\Gamma(a_1)\Gamma(a_2)}{\Gamma(a_3)\Gamma(a_4)}, \tag{22}$$

with

$$a_1 = (3p + 19)/12, \tag{23}$$

$$a_2 = (3p - 1)/12, \tag{24}$$

$$a_3 = (3p + 2)/12, \tag{25}$$

$$a_4 = (3p + 22)/12. \tag{26}$$

Using $p_0 = 2$ and Equation (14), the expressions for the synchrotron emission coefficient, opacity, and source function reduce to

$$j_\nu^{\rm s} = 2.3 \times 10^{-15} \left(\frac{C_\gamma}{10^{10}}\right) B^{3/2}\ \lambda^{1/2}, \tag{27}$$

$$(\kappa_\nu \rho)^{\rm s} = 5.1 \times 10^{-11} \left(\frac{C_\gamma}{10^{10}}\right) B^2\ \lambda^3, \tag{28}$$

$$S_\nu^{\rm s} = 4.5 \times 10^{-5}\, B^{-1/2}\ \lambda^{-5/2}. \tag{29}$$

It is possible to develop an "effective photosphere" analysis for pure, optically thick synchrotron radiation, following the approach of Cassinelli & Hartmann (1977). Details of the full solution and the approximation of an effective photosphere are given in Appendix A. With Equation (16), and a field strength that declines like a toroid[4] with

$$B(r) = B_* \left(\frac{R_*}{r}\right), \tag{30}$$

where the "*" notation indicates a value at the base of the stellar wind, the extent of the radio photosphere will then scale as $R_\nu \propto \lambda^{3/(3+m)}$. The corresponding specific radio luminosity becomes $L_\nu \propto S_\nu R_\nu^2 \propto \lambda^{-5m/(6+2m)}$. For a choice of $m = 2$ in C_γ, the photospheric radius will grow as $R_\nu \sim \lambda^{0.6}$, close to the value for free–free emission. However, the SED slope is somewhat steeper than the case of free–free emission, with $L_\nu \propto \lambda^{-1}$. We note that for large values of m, the radius of the synchrotron radio photosphere approaches a constant with wavelength, and the SED steepens to $L_\nu \sim \lambda^{-2.5}$. However, there are other factors that influence the SED, such as Razin suppression, addressed below.

2.3. The Razin Effect

The Razin effect (e.g., Dougherty et al. 2003) refers to the suppression of synchrotron emission due to the refractive index of the plasma. It is dependent on the plasma frequency, and the frequency at which the effect becomes important is given by (e.g., Van Loo et al. 2004):

$$\nu_R = 20 \frac{n_e}{B}. \tag{31}$$

The suppression of the synchrotron emission scales as $\approx e^{-\nu_R/\nu} = e^{-\lambda/\lambda_R}$, where $\lambda_R = c/\nu_R$. At frequencies lower than ν_R (or wavelengths longer than λ_R), the synchrotron emission is strongly reduced.

It is useful to develop a scale of where in the wind the Razin effect becomes significant. To provide an estimate, we assume the electron density decreases as r^{-2}, and the field strength decreases as r^{-1}. With a wind density of $n_0 = 10^{13}\,{\rm cm}^{-3}$, and a stellar field strength of $B_* = 100$ G, Equation (31) gives $\lambda_R = 1$ cm at a radius of $r_R \approx 70 R_*$. At larger radii, the Razin wavelength will be greater. Consequently, for an observation wavelength of 1 cm, the Razin effect will suppress synchrotron emission for $r < r_R$, but not for $r > r_R$.

3. SEDs from Winds with Free–Free and Synchrotron Emission

We now consider an ionized and magnetized wind that is spherically symmetric, with both free–free and synchrotron opacities. The source function is

$$S_\nu = \frac{j_\nu^{\rm ff} + j_\nu^{\rm s}}{(\kappa_\nu \rho)^{\rm ff} + (\kappa_\nu \rho)^{\rm s}}. \tag{32}$$

Except for very long wavelengths or very large distances in the wind, it is reasonable to expect that the synchrotron opacity is considerably smaller than the free–free opacity (Appendix A),

[4] With flux freezing for highly ionized winds, rotation generally leads to a toroidal field topology (e.g., Ignace et al. 1998).

so that the source function reduces to

$$S_\nu = B_\nu(T) + \frac{j_\nu^{\rm s}}{(\kappa_\nu \rho)^{\rm ff}}, \tag{33}$$

with the free–free opacity $(\kappa_\nu \rho)^{\rm ff}$ (Equation (4)) as the sole contributor to the absorption coefficient.

From Equation (6), the optical depth of the thermal absorption is the LOS integral of the free–free opacity, along a constant impact parameter. The expression is analytic, and integrates to

$$\tau_\nu^{\rm ff} = \frac{\tau_0}{2}\, u^3\, g_\nu^{\rm ff} \left(\frac{\lambda}{\lambda_0}\right)^2 \left(\frac{\theta - \mu \sin\theta}{\sin^3\theta}\right), \tag{34}$$

where $\cos\theta = \mu$, $\sin\theta = \varpi u$, and $u = R_*/r$. The angle θ varies over a range of $[0, \pi]$, with $\theta < \pi/2$ describing the hemisphere of the observer. For simplicity, we have defined the constant

$$\tau_0 = 2 \times 10^8 \frac{Z_{\rm i}^2}{\mu_{\rm i}\, \mu_{\rm e}} \left(\frac{R_*}{10^{11}}\right) \left(\frac{n_0}{10^{13}}\right)^2 \left(\frac{10^4}{T}\right)^{3/2}. \tag{35}$$

With these quantities, and ignoring any radio emission from the star itself, the formal solution for a radio SED from an isothermal wind is

$$L_\nu = 8\pi^2 R_*^2 \left\{ B_\nu \int_0^\infty [1 - e^{-\tau_{\rm tot}(\varpi)}]\, \varpi\, d\varpi + \int_0^\infty \int_0^{\tau_{\rm tot}(\varpi)} \frac{j_\nu^{\rm s}}{(\kappa_\nu \rho)^{\rm ff}}\, e^{-\tau_\nu^{\rm ff}}\, \varpi\, d\tau_\nu^{\rm ff}\, d\varpi \right\}, \tag{36}$$

where $\tau_{\rm tot} = \tau_\nu^{\rm ff}(\varpi, \theta \to \pi)$, and we have ignored any contribution from the stellar disk. Note that we ignore Razin suppression of the synchrotron emission in this expression, which will be discussed below.

The first integral in Equation (36) can be evaluated analytically as

$$\begin{aligned} L_\nu &= 8\pi^2 R_*^2\, B_\nu \int_0^\infty [1 - e^{-\tau_{\rm tot}(\varpi)}]\, \varpi\, d\varpi \\ &= 8\pi^2 R_*^2\, B_\nu \int_0^\infty [1 - e^{-\zeta \varpi^{-3}}]\, \varpi\, d\varpi \\ &= 4\pi^2 R_*^2\, B_\nu\, \Gamma\left(\frac{1}{3}\right) \left(\frac{\pi}{2}\, \tau_0 \left(\frac{\lambda}{\lambda_0}\right)^2\right)^{2/3}, \end{aligned} \tag{37}$$

where in the second equality we have used

$$\begin{aligned} \tau_{\rm max}(\varpi) &= \int_{-\infty}^{\infty} (\kappa_\nu \rho)^{\rm ff} dz \\ &= \frac{\pi\, \tau_0}{2\, \varpi^3} \left(\frac{\lambda}{\lambda_0}\right)^2, \end{aligned} \tag{38}$$

with $\zeta = \pi \tau_0 \lambda^2 / 2\lambda_0^2$. Using the appropriate approximation for B_ν in the Rayleigh–Jeans limit, this expression can be recast as

$$L_\nu = L_0 \left(\frac{\lambda}{\lambda_0}\right)^{-2/3}, \tag{39}$$

with

$$L_0 = 1.35 \times 10^{18} \left(\frac{Z_{\rm i}^2}{\mu_{\rm e}\, \mu_{\rm i}}\right)^{2/3} \left(\frac{n_0}{10^{13}}\right)^{4/3} \left(\frac{R_*}{10^{11}}\right)^{8/3} \tag{40}$$

as the scaling for the specific luminosity, with units of erg s^{-1} Hz^{-1}. For the sake of illustrative models, we ignore the wavelength dependence of the free–free factor and set $g_\nu^{\rm ff} = 1$, yielding $L_\nu \propto \lambda^{-2/3}$. The inclusion of $g_\nu^{\rm ff}$ would produce the canonical $L_\nu \propto \lambda^{0.6}$ result.

The second integral in Equation (36) can be recast as

$$L_\nu = 8\pi^2\, R_*^3\, j_0 \int_{-1}^{1} \int_0^1 \left(\frac{\lambda}{\lambda_0}\right)^{1/2} u^{m-1/2}\, e^{-\tau_\nu^{\rm ff}} du\, d\mu, \tag{41}$$

where we have applied Equation (27), assuming $p = 2$, and the constant $j_0 = 2.3 \times 10^{-25}\, B_*^{3/2} C_*$.

For the case of $m = 1/2$, for an optically thick wind ($\tau_0 \gg 1$), Equation (41) can be solved analytically to express the wavelength dependence of the SED:

$$\begin{aligned} L_\nu &= 8\pi^2\, R_*^3\, j_0 \left(\frac{\lambda}{\lambda_0}\right)^{1/2} \int_{-1}^{1} \int_0^\infty e^{-\tau_\nu^{\rm ff}} du\, d\mu \\ &= L_0\, K_0 \left(\frac{\lambda}{\lambda_0}\right)^{-1/6} \left(\frac{2}{\tau_0}\right)^{1/3} \Gamma\left(\frac{4}{3}\right) \Lambda_0, \end{aligned} \tag{42}$$

where

$$\Lambda_0 = \int_{-1}^{+1} \frac{\sin\theta}{(\theta - \cos\theta \sin\theta)^{1/3}}\, d\mu = \frac{3\pi^{2/3}}{4}, \tag{43}$$

and the constant K_0 is equal to

$$\begin{aligned} K_0 &= \frac{8\pi^2 j_0 R_*^3}{L_0} \\ &= 1.35 \times 10^5 \left(\frac{C_*}{10^{10}}\right) \left(\frac{R_*}{10^{11}}\right)^{1/3} \left(\frac{B_*}{100\ {\rm G}}\right)^{3/2} \\ &\quad \times \left(\frac{Z_{\rm i}^2}{\mu_{\rm e}\, \mu_{\rm i}}\right)^{-2/3} \left(\frac{n_0}{10^{13}}\right)^{-4/3}. \end{aligned} \tag{44}$$

Here, we have applied a fiducial scaling for the surface magnetic field B_*. We note that K_0 is dependent on a number of parameters, especially considering that n_0 (Equation (9)) also depends on the stellar $\dot{M}$, R_*, and v_∞. Thus, a given K_0 may apply to a wide combination of observables. Table 1 lists the values of K_0 considered for our model SEDs.

Table 1
Model Parameters for the SEDs Shown in Figure 1

m	0.0, 0.5, 1.0
$K_0(m = 0.0)$	1
$K_0(m = 0.5)$	100
$K_0(m = 1.0)$	30,000
a_0	0 (no Razin), 1, 3, 9, 27, 81

Note. The dimensionless constant a_0 is used to parameterize the Razin wavelength, as $\lambda_{\rm R} = \lambda_{\rm R}^0 / a_0$ (see also Equation (47)). Choosing a value of $B_* = 100$ G, $K_0 \sim 100$ for typical WR star parameters, and $K_0 \sim 20$ for the typical parameters associated with an O supergiant.

The formal solution is then

$$\frac{L_\nu}{L_0} = \left(\frac{\lambda}{\lambda_0}\right)^{-2/3} + 1.4\, K_0 \left(\frac{2}{\tau_0}\right)^{1/3} \left(\frac{\lambda}{\lambda_0}\right)^{-1/6}. \tag{45}$$

While this result is essentially unphysical, since at sufficiently long wavelengths the luminosity integrated over

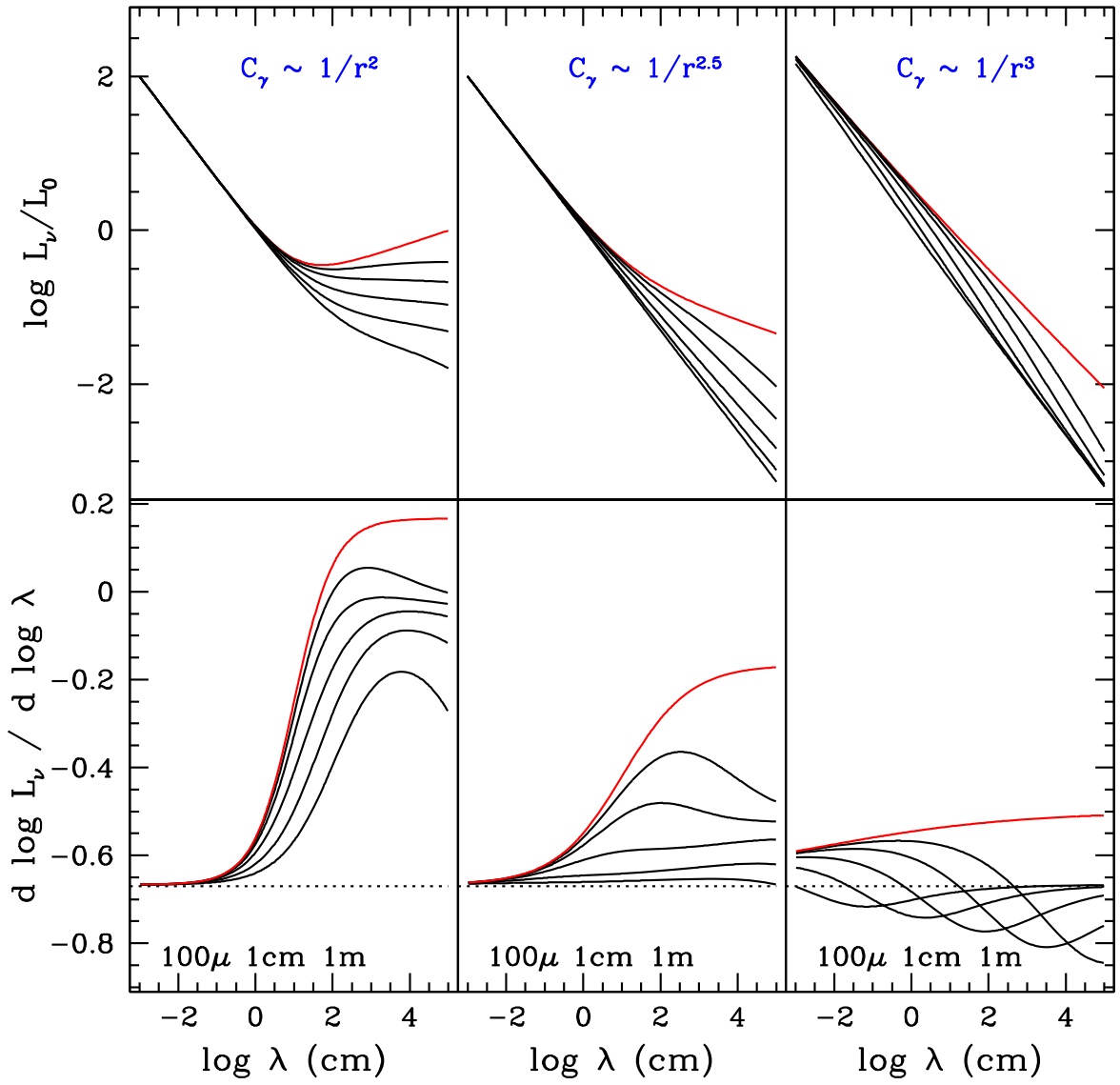

Figure 1. The upper panels show model SEDs; the lower panels show logarithmic slopes of the SEDs with wavelength, representing the instantaneous power-law exponent. At short wavelengths, where the slope is −2/3 (the dotted lines), the SED is dominated by the free–free emission. Deviations from that value signify the influence of synchrotron emission. The rows from left to right show different radial distributions of the relativistic electron population density, as represented by C_γ. The red curve in each case indicates a model that does not include the Razin effect (corresponding to the model parameter $a_0 = 0$). Each successive curve below is a model with a larger value of a_0, corresponding to increasingly more suppression of the synchrotron emission. The model parameters are provided in Table 1. Consistent with the discussion in Section 2.2, we have used a power-law index of $p(r) = p_0 = 2$.

wavelength is unbounded, Equation (45) is useful for illustrating the transition of the SED from a thermal to a nonthermal spectrum. Model SEDs without the Razin suppression of the synchrotron emission (i.e., $a_0 = 0$) are shown as the red curves in Figure 1. These models show that the radio spectrum follows the curve expected from thermal emission at short wavelengths, but then becomes modified by the synchrotron emission at long wavelengths.

Including the Razin effect (suppressing synchrotron emission) in the formal solution yields

$$\frac{L_\nu}{L_0} = \left(\frac{\lambda}{\lambda_0}\right)^{-2/3} + K_0\left(\frac{\lambda}{\lambda_0}\right)^{1/2} \times \int_{-1}^{1}\int_{0}^{1} u^{m-1/2}\, e^{-\tau_\nu(u,\mu)}\, e^{-\lambda/\lambda_R(u)}\, du\, d\mu, \quad (46)$$

where $\lambda_R(u) = \lambda_R^0/u$ is the Razin wavelength (Equations (30) and (31)). The Razin wavelength scale constant is defined as

$$\lambda_R^0 = 0.015 \text{ cm } \frac{B_*}{100 \text{ G}} \frac{10^{13}}{n_0}. \quad (47)$$

Figure 1 also shows model SEDs that include the Razin effect (the black curves). The inclusion of Razin suppression significantly diminishes the synchrotron component at long wavelengths.

4. Discussion

The synthetic SEDs shown in Figure 1 indicate that the inclusion of synchrotron emission can have a significant impact on the shape of the long-wavelength SED, even when Razin suppression is considered. In this regime, the SED is no longer

dominated by thermal free–free emission, and so deviates from the canonical power-law slope. This change is most pronounced when there is a fixed, constant ratio between the wind density and the number density of relativistic electrons (left column).

For steeper distributions of relativistic electrons, the wavelength at which the free–free emission ceases to dominate the SED decreases. Razin suppression of the synchrotron emission becomes more pronounced, producing an SED with a slope that closely resembles the thermal power-law result. This implies that a sufficiently steep distribution of relativistic electrons may produce an SED with a power-law slope that mimics the result for thermal emission, particularly in a given wave band.

Our results indicate that, in the absence of other factors, synchrotron emission can influence single-star SEDs, although a relatively fine degree of wavelength sampling may be needed for the detection of the effect owing to the gradual change in SED slope. Although we do not directly consider magnetic massive stars as part of this analysis, we briefly explore the effect of a latitudinally dependent toroidal field on the shape of the SED in Appendix B.

The models reported here explore different distributions for the population of relativistic electrons using a power-law prescription for C_γ, although we offer no model for either how or where electrons are accelerated or transported throughout the wind. Indeed, the processes through which nonthermal synchrotron emission is produced in single massive stars are still unclear. For stars with sufficient mass-loss rates to produce radio excesses in the wind, but with only modest surface magnetic fields (well below 1 kG), the radio photosphere is relatively extended compared to where synchrotron emission would typically form in the inner wind. As a result, little of the nonthermal component should escape to be observable. In order for nonthermal emission to compete in amplitude with the thermal component, electrons would need to be accelerated at relatively large radii of $\sim 10^1 - 10^2 R_*$.

Wind clumping may provide one pathway to achieving nonthermal emission in the extended stellar wind of a single massive star. The wind instabilities commonly understood to be associated with clumping give rise to shocks that are spread throughout the wind outflow. Such shocks have generally been associated with X-ray production (e.g., Berghoefer et al. 1997; Nazé et al. 2011), and thus are a natural environment where electrons could be accelerated to relativistic energies (e.g., White 1985; Chen & White 1994). For example, XMM-Newton and Chandra observations of the Wolf–Rayet star WR 6[5] show evidence for X-ray-emitting hot plasma emerging from $\sim 30 R_*$ in the wind (Oskinova et al. 2012; Ignace et al. 2013; Huenemoerder et al. 2015), suggesting that shocks could form or persist to large radii.

More work will be needed to determine the role of wind instabilities in the production of nonthermal emission. Fully 3D simulations of the wind-driving instability mechanism have not yet been performed, although 2D simulations have been reported (e.g., Dessart & Owocki 2003; Sundqvist et al. 2018). A recent study by Sundqvist & Puls (2018) has suggested that porosity effects do not impact the radio photosphere of O-type stars. However, as Van Loo et al. (2006) point out, the results of 2D simulations inform our view of how shocks form and propagate outward in the wind. In particular, the 2D simulations indicate that round structures can form,[6] which stands in opposition to the frequently invoked "pancake" shock geometry, referring to a shell that breaks up into multiple fragments of modest or small solid angle.

It is not yet clear how fully 3D simulations of the time-dependent wind flow would alter the expectations for particle acceleration. However, Ignace (2016) considered how porosity could impact the thermal radio emission in dense winds by including spherical clumps. Although it presents a simplistic model in some respects, that study determined that porosity with spherical clumps implied that the radio photosphere forms deeper in the wind, as compared to the pure microclumping scenario. This may alleviate, to some extent, the distance to which relativistic electrons must survive or be accelerated in order for synchrotron emission to be significant.

The magnetospheres of single magnetic massive stars provide another environment in which nonthermal emission can be produced. The confinement and channeling of the stellar wind by the magnetic field leads to the production of X-ray emission from shocks (e.g., Babel & Montmerle 1997a; ud-Doula & Owocki 2002; Gagné et al. 2005; Oskinova et al. 2011a, 2011b; Nazé et al. 2014; ud-Doula & Nazé 2016), which can accelerate electrons to the energies necessary for synchrotron emission. Babel & Montmerle (1997b) used their model for magnetically confined wind shocks (MCWSs) to describe the X-ray emission of IQ Aur (HD 34452; A0p), and suggested that the model could also be generally applied to the nonthermal radio emission from chemically peculiar A- and B-type (ApBp) stars. In this scenario, relativistic electrons are produced via a second-order Fermi acceleration mechanism, leading to the observed synchrotron emission. Trigilio et al. (2004) reported an alternate model for magnetic chemically peculiar stars, suggesting that electrons are accelerated to relativistic speeds in current sheets that develop in the "middle magnetosphere" (where the stellar wind breaks open the magnetic field loops), while thermal-emitting plasma is trapped in the "inner magnetosphere" (the region within the closed magnetic field loops).

Recently, Leto et al. (2021) and Shultz et al. (2022) have proposed an alternate mechanism for the production of nonthermal emission in massive star magnetospheres. In contrast to the model developed by Trigilio et al. (2004), these authors argue for the production of synchrotron emission from a shellular "radiation belt" within the inner magnetosphere. The existence of such a structure appears to be supported by observational evidence (Shultz et al. 2022).

The theoretical framework for how electrons are accelerated to relativistic energies in single massive stars will need to be refined. Yet there is observational evidence for free–free and nonthermal emission in single massive stars, particularly among the magnetic early-type star population. Thus, there is a pressing need for additional multiwavelength observations of radio SEDs, in order to further characterize this population.

The models reported here can be used to help predict and interpret the behavior of radio SEDs from single massive stars. In terms of the emissive model, future developments of this

[5] Schmutz & Koenigsberger (2019) have claimed that WR 6 may have a binary companion, which then could account for X-rays from large radii. In an independent analysis, St-Louis et al. (2020) have not been able to confirm the claim. Moreover, the resolved X-ray line profile shapes observed by Huenemoerder et al. (2015) are consistent with predictions for a spherically symmetric terminal speed flow (Ignace 2001).

[6] Formally, these are rings in the 2D simulations; one may naturally expect spheroidal structures to form in fully 3D models.

work would include exploring the effects of an aspherical wind density, plus a consideration of the pitch-angle effects for the relativistic electrons. Also needed is further work on the acceleration of electrons to relativistic energies and their distribution throughout the wind. These improvements are necessary to produce more quantitative predictions for SEDs involving both free–free and synchrotron contributions.

The authors wish to thank the anonymous referee for their careful reading and helpful comments, which have contributed to the final version of this paper.

C.E. and R.I. gratefully acknowledge that this material is based upon work supported by the National Science Foundation under grant number AST-2009412.

Appendix A
Approximation of an Effective Photosphere for Synchrotron Emission

We develop here an "effective photosphere" analysis for pure, optically thick synchrotron radiation, using the method outlined in Cassinelli & Hartmann (1977).

The optical depth of a location in the wind is given by the integral of the synchrotron opacity (Equation (28)) along the observer's line of sight. From Section 2.2, the field strength is described by Equation (30), and we apply a constant power-law index of $p(r) = p_0 = 2$, so that the expression for the optical depth is written as

$$\tau_\nu^{\rm s} = \int (\kappa_\nu \rho)^{\rm s}\, dz, \\ = \tau_0^{\rm s}\, R_*^{3+m} \left(\frac{\lambda}{\lambda_0}\right)^3 \int_0^{\theta_0(\varpi)} \frac{(\sin\theta)^{2+m}}{\varpi^{3+m}} d\theta, \quad \text{(A1)}$$

where, in the second equality above, we have applied the change of variable $z = \varpi \cot\theta$, where ϖ is the impact parameter, and θ gives the angle between the radial direction and the observer's LOS. For simplicity, we also define the quantity

$$\tau_0^s = 5.1 \times 10^{-11}\, B_*^2\, R_* \left(\frac{C_*}{10^{10}}\right). \quad \text{(A2)}$$

Under the assumption that $R_\nu \gg R_*$, $\theta_0 = \pi$, and the expression for the optical depth can be evaluated analytically,

$$\tau_\nu^{\rm s} = \sqrt{\pi}\ \tau_0^{\rm s} \left(\frac{\lambda}{\lambda_0}\right)^3 \left(\frac{R_*}{\varpi}\right)^{3+m} \frac{\Gamma(\frac{3+m}{2})}{\Gamma(\frac{4+m}{2})}. \quad \text{(A3)}$$

For the choice of $m = 0$, this yields

$$\tau_\nu^{\rm s} = \frac{\pi}{2}\, \tau_0^{\rm s} \left(\frac{\lambda}{\lambda_0}\right)^3 \left(\frac{R_*}{\varpi}\right)^3. \quad \text{(A4)}$$

Using Equations (34) and (35) for the free–free optical depth, Equations (A2) and (A4) for the synchrotron optical depth, the fiducial values given throughout this paper, and a choice of $\theta = \pi/2$, we find $\tau_\nu^{\rm s}/\tau_\nu^{\rm ff} \sim 10^{-4}$.

Equation (A3) shows that the optical depth from pure synchrotron radiation increases more strongly with wavelength than the optical depth from free–free radiation (Equation (34)) alone. As discussed in Section 2.2, the synchrotron radio photosphere will vary as $R_\nu^{\rm s} \propto \lambda^{3/(3+m)}$. For $m = 0$, $R_\nu^{\rm s} \propto \lambda$, with a stronger dependence on wavelength than the free–free radio photosphere, which grows as $R_\nu \propto \lambda^{2/3}$ (Equation (8)). However, for $m = 2$, the synchrotron effective radius of $R_\nu^{\rm s} \sim \lambda^{0.6}$ has a similar scaling to that for pure free–free radiation.

Appendix B
Solution for a Latitudinal Dependence of the Toroidal Field

There are three primary effects that can lead to deviations from spherical symmetry in relation to the approach adopted in this paper:

1. the magnetic field has both a latitudinal and an azimuthal dependence for strength and direction;
2. the pitch angles of the relativistic electrons are not random; and
3. the wind density itself is not spherically symmetric.

Here, we only address the first point. Although this condition likely implies the third point, we assume that the wind density is spherically symmetric, in order to isolate the effects of the field topology.

For synchrotron radiation formed in a wind that is thick to free–free opacity (Appendix A), at a radius far from the stellar surface, a toroidal component of the magnetic field is most relevant, due to its slow decline with radius as r^{-1}. One may reasonably expect a latitudinal dependence of the field, with

$$B_\varphi = \pm B_* \sin\vartheta \left(\frac{R_*}{r}\right) = \pm B_* \sin\vartheta \times u, \quad \text{(B1)}$$

where $\pm B_*$ is the magnetic field strength at the stellar surface, and ϑ and φ are spherical angular coordinates defined by the axis of symmetry for the toroidal field.

We define the observer's coordinates (θ, α) with respect to the LOS view that is inclined by angle i to the field symmetry axis. Thus, $i = 0°$ gives a magnetic pole-on view, and $i = 90°$ gives an "edge-on" view of the magnetic equator. The coordinate transformation between the observer's (θ, α) and the latitude ϑ for the field is given by spherical trigonometry, with

$$\cos\vartheta = \cos\theta \cos i + \sin\theta \sin i \cos\alpha. \quad \text{(B2)}$$

The free–free optical depth to a point (r, θ) in the wind is given by Equation (34):

$$\tau_\nu^{\rm ff}(u, \theta) = \frac{\tau_0\, u^3}{2} \left(\frac{\lambda}{\lambda_0}\right)^2 \left(\frac{\theta - \cos\theta \sin\theta}{\sin^3\theta}\right). \quad \text{(B3)}$$

The Razin wavelength now becomes

$$\lambda_R(u, \mu) = \lambda_{\rm R}^0 \sin\vartheta\ u^{-1}, \quad \text{(B4)}$$

where the constant $\lambda_{\rm R}^0$ is given by Equation (47).

The luminosity of the radio emission, including both free–free and synchrotron processes, for a toroidal magnetic field with a latitudinal component, is then

$$\frac{L_\nu}{L_0} = \left(\frac{\lambda}{\lambda_0}\right)^{-2/3} + \frac{K_0}{2\pi} \left(\frac{\lambda}{\lambda_0}\right)^{1/2} \\ \times \int u^{m-1/2} (\sin\vartheta)^{3/2}\ e^{-\tau_{\nu,\rm ff}}\ e^{-\lambda/\lambda_R}\, du\, d\mu\, d\alpha, \quad \text{(B5)}$$

where $\vartheta = \vartheta(\mu, \alpha)$ and $\lambda_R = \lambda_R(u, \mu, \alpha)$. The evaluation of the integral requires the elimination of ϑ in terms of θ and α, using Equation (B2). The result will therefore depend on the viewing inclination, giving a luminosity that depends on i. Figure 2

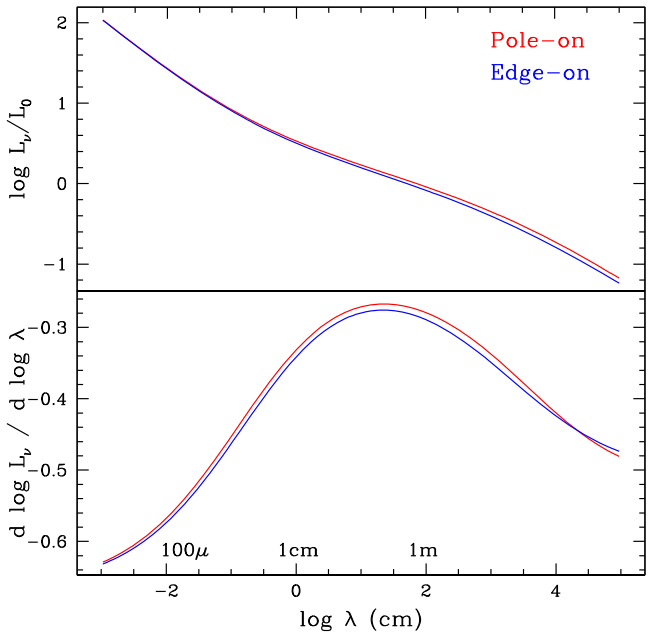

Figure 2. The luminosity of the radio emission from both free–free and synchrotron processes, assuming a toroidal magnetic field with latitudinal dependence. The model assumes $K_0 = 200$, $m = 0.5$, and $a = 3$. We show the resultant SEDs for inclinations of 0° (a pole-on view; red curves) and 90° (an edge-on view; blue curves).

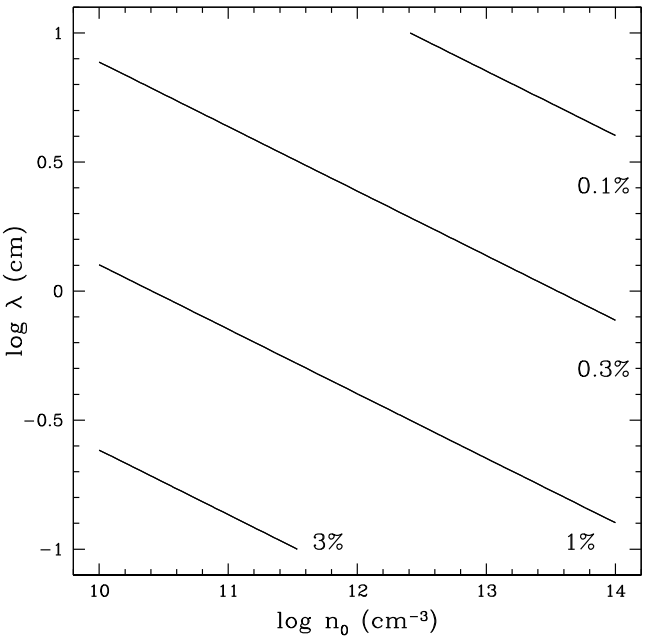

Figure 3. Contour plot of the percent error in optical depth (Equation (C4)). The axes are the wind density scale n_0 and wavelength λ.

shows the results for calculations with $K_0 = 200$, $m = 0.5$, and $a = 3$, contrasting a pole-on view of $i = 0°$ (the red curves) with an edge-on view of $i = 90°$ (the blue curves).

Figure 2 reveals that including a latitudinal dependence of the toroidal field has a fairly minimal impact on the SED shape or the brightness level. However, if considered in conjunction with a nonspherical density, the effects could more substantial. An adjustment of the model to include a nonspherical density will be challenging. An axisymmetric density will introduce at least two more free parameters: a density contrast and a distribution of density with latitude. Additionally, the free–free optical depth would no longer be generally analytic, meaning that a greater computational expense would be required to explore the range of outcomes with multiple model parameters.

Appendix C
Applicability of Constant Expansion

This contribution has explored how synchrotron emission can alter the SED shape formed by a wind that is optically thick to thermal free–free opacity. As discussed above, high opacity results from a combination of dense winds and long-wavelength radiation, and the canonical SED shape is a power law with $f_\nu \propto \lambda^{-2/3}$ (using the assumption for the Gaunt Factor of $g_\nu^{\rm ff} = 1$ adopted throughout this work). This result assumes a spherical, constantly expanding wind. Here, we comment on the applicability of this assumption.

Consider a canonical wind velocity law with $\beta = 1$, such that $v(r) = v_\infty(1 - R_*/r)$. In normalized form, applying the substitution $u = R_*/r$, the velocity law can be expressed as $w(u) = 1 - u$. The optical depth to any location u in the wind (Equation (6)) is then

$$\tau^{\rm ff}(u) = \tau_0\left[\frac{1}{(1-u)} - (1-u) + 2\ln(1-u)\right], \qquad \text{(C1)}$$

with

$$\tau_0 = 1.99 \times 10^8\left(\frac{\lambda}{\lambda_0}\right)^2\left(\frac{n_0}{10^{13}}\right)^2\left(\frac{R_*}{10^{11}}\right)g_\nu^{\rm ff}. \qquad \text{(C2)}$$

We note that while $\tau^{\rm ff}$ is an analytic function of u, the determinate of $u(\tau^{\rm ff})$ is implicit, requiring root finder methods for a solution.

For constant expansion, the characteristic radius of the free–free photosphere (Equation (8)) is then

$$u_\nu = \frac{R_*}{R_\nu} \equiv \left(\frac{\tau_0}{3}\right)^{1/3}, \qquad \text{(C3)}$$

where the location u_ν has been defined by the condition of optical unity (Equation (7)).

One way to assess the applicability of our assumptions is to evaluate $\tau^{\rm ff}(u_\nu)$ using Equation (C1). We define the relative error in the approximation for the optical depth as

$$\text{Error} = 100\% \times \left(\frac{\tau^{\rm ff}(u) - 1}{\tau^{\rm ff}(u)}\right). \qquad \text{(C4)}$$

Figure (3) provides a contour plot of this error. For simplicity, we assume a constant stellar luminosity L_*, and have adopted the scaling relations for hot massive star winds from Vink (2021), with $\dot{M} \propto L_*^{2.2}\, M_*^{-1.3}\, T_*$ for stellar mass and effective temperature M_* and T_*, respectively (see Equation (4) of that paper). We assume for massive stars that $M_* \propto L_*$, and constant luminosity implies $T_* \propto R_*^{-1/2}$. For the wind terminal speed, $v_\infty \propto v_{\rm esc} \propto M_*^{1/2}\, R_*^{-1/2}$. We apply these scaling relations to Equation (9) to obtain the wind density scale n_0 in terms of these quantities,

$$n_0 \propto \frac{\dot{M}}{R_*^2\, v_\infty} \propto \frac{L_*^{0.9}}{R_*^2\, M_*^{1/2}} \propto \frac{L_*^{0.4}}{R_*^2}. \qquad \text{(C5)}$$

Since the most luminous stars tend to have the highest wind mass-loss rates, the assumption of a constant L_* implies $R_* \propto n_0^{1/2}$, and thus $\tau_0 \propto \lambda^2\, n_0^{3/2}$. This is the scaling relation used in Figure 3. While crude, the relation indicates that lower wind densities correspond to larger stars. For example, a wind density scale of $n_0 = 10^{13}\,\mathrm{cm}^{-3}$ and a stellar radius $R_* = 10^{11}\,\mathrm{cm} \sim 1.5\,R_\odot$ is appropriate to describe a WR star. In contrast, under our assumptions, a density scale of $n_0 = 10^{10}\,\mathrm{cm}^{-3}$ (appropriate for an O supergiant) would have a corresponding stellar radius of $R_* \sim 45\,R_\odot$ (which, in reality, is about a factor of 2 too large). Overall, Figure 3 reveals that across the span of wind density scales appropriate to stars ranging from O supergiants to WRs, at wavelengths from around 10 cm to 1 mm, the approximation of constant expansion is quite good. We find a maximum error in the optical unity assumption of ∼5%, for $\lambda = 1$ mm with $n_0 = 10^{10}\,\mathrm{cm}^{-3}$.

ORCID iDs

Christiana Erba https://orcid.org/0000-0003-1299-8878
Richard Ignace https://orcid.org/0000-0002-7204-5502

References

Abbott, D. C., Beiging, J. H., Churchwell, E., & Torres, A. V. 1986, ApJ, 303, 239
Abbott, D. C., Bieging, J. H., & Churchwell, E. 1981, ApJ, 250, 645
Abbott, D. C., Bieging, J. H., Churchwell, E., & Cassinelli, J. P. 1980, ApJ, 238, 196
Alecian, E., Kochukhov, O., Petit, V., et al. 2014, A&A, 567, A28
Babel, J., & Montmerle, T. 1997a, ApJL, 485, L29
Babel, J., & Montmerle, T. 1997b, A&A, 323, 121
Benaglia, P., Marcote, B., Moldón, J., et al. 2015, A&A, 579, A99
Berghoefer, T. W., Schmitt, J. H. M. M., Danner, R., & Cassinelli, J. P. 1997, A&A, 322, 167
Bieging, J. H., Abbott, D. C., & Churchwell, E. B. 1989, ApJ, 340, 518
Blomme, R., Fenech, D. M., Prinja, R. K., Pittard, J. M., & Morford, J. C. 2017, A&A, 608, A69
Blomme, R., & Runacres, M. C. 1997, A&A, 323, 886
Bromm, V., & Larson, R. B. 2004, ARA&A, 42, 79
Brussaard, P. J., & van de Hulst, H. C. 1962, RvMP, 34, 507
Cassinelli, J. P., & Hartmann, L. 1977, ApJ, 212, 488
Chen, W., & White, R. L. 1991, ApJ, 366, 512
Chen, W., & White, R. L. 1994, Ap&SS, 221, 259
Daley-Yates, S., Stevens, I. R., & ud-Doula, A. 2019, MNRAS, 489, 3251
De Becker, M. 2018, BSRSL, 87, 185
De Becker, M., Benaglia, P., Romero, G. E., & Peri, C. S. 2017, A&A, 600, A47
Dessart, L., & Owocki, S. P. 2003, A&A, 406, L1
Donati, J. F., Howarth, I. D., Jardine, M. M., et al. 2006, MNRAS, 370, 629
Donati, J.-F., & Landstreet, J. D. 2009, ARA&A, 47, 333
Dougherty, S. M., Pittard, J. M., Kasian, L., et al. 2003, A&A, 409, 217
Dougherty, S. M., & Williams, P. M. 2000, MNRAS, 319, 1005
Eichler, D., & Usov, V. 1993, ApJ, 402, 271
Ellison, D. C., & Eichler, D. 1985, PhRvL, 55, 2735
Falceta-Gonçalves, D., & Abraham, Z. 2012, MNRAS, 423, 1562
Fossati, L., Castro, N., Schöller, M., et al. 2015, A&A, 582, A45
Fullerton, A. W., Massa, D. L., & Prinja, R. K. 2006, ApJ, 637, 1025
Gagné, M., Oksala, M. E., Cohen, D. H., et al. 2005, ApJ, 628, 986
Grunhut, J. H., Wade, G. A., Neiner, C., et al. 2017, MNRAS, 465, 2432
Heger, A., Fryer, C. L., Woosley, S. E., Langer, N., & Hartmann, D. H. 2003, ApJ, 591, 288
Heger, A., & Woosley, S. E. 2010, ApJ, 724, 341
Hopkins, P. F., Quataert, E., & Murray, N. 2012, MNRAS, 421, 3522
Huenemoerder, D. P., Gayley, K. G., Hamann, W. R., et al. 2015, ApJ, 815, 29
Hummer, D. G. 1988, ApJ, 327, 477
Ignace, R. 2001, ApJL, 549, L119
Ignace, R. 2016, MNRAS, 457, 4123
Ignace, R., Cassinelli, J. P., & Bjorkman, J. E. 1998, ApJ, 505, 910
Ignace, R., Gayley, K. G., Hamann, W. R., et al. 2013, ApJ, 775, 29
Ignace, R., Quigley, M. F., & Cassinelli, J. P. 2003, ApJ, 596, 538
Klement, R., Carciofi, A. C., Rivinius, T., et al. 2017, A&A, 601, A74
Kochukhov, O., Lundin, A., Romanyuk, I., & Kudryavtsev, D. 2011, ApJ, 726, 24
Kurapati, S., Chandra, P., Wade, G., et al. 2017, MNRAS, 465, 2160
Lamers, H. J. G. L. M., & Cassinelli, I. P. 1996, in ASP Conf. Ser. 98, From Stars to Galaxies: the Impact of Stellar Physics on Galaxy Evolution, ed. C. Leitherer, U. Fritze-von-Alvensleben, & J. Huchra (San Francisco, CA: ASP), 162
Langer, N. 2012, ARA&A, 50, 107
Leitherer, C., Chapman, J. M., & Koribalski, B. 1995, ApJ, 450, 289
Leitherer, C., Chapman, J. M., & Koribalski, B. 1997, ApJ, 481, 898
Leto, P., Trigilio, C., Buemi, C. S., Umana, G., & Leone, F. 2006, A&A, 458, 831
Leto, P., Trigilio, C., Krtička, J., et al. 2021, MNRAS, 507, 1979
Leto, P., Trigilio, C., Oskinova, L., et al. 2017, MNRAS, 467, 2820
Leto, P., Trigilio, C., Oskinova, L. M., et al. 2018, MNRAS, 476, 562
Lucy, L. B., & White, R. L. 1980, ApJ, 241, 300
Madau, P., & Dickinson, M. 2014, ARA&A, 52, 415
Morel, T., Castro, N., Fossati, L., et al. 2015, in IAU Symp. 307, New Windows on Massive Stars, ed. G. Meynet et al. (Cambridge: Cambridge Univ. Press), 342
Nazé, Y., Broos, P. S., Oskinova, L., et al. 2011, ApJS, 194, 7
Nazé, Y., Petit, V., Rinbrand, M., et al. 2014, ApJS, 215, 10
Nugis, T., Crowther, P. A., & Willis, A. J. 1998, A&A, 333, 956
Oskinova, L. M., Gayley, K. G., Hamann, W. R., et al. 2012, ApJL, 747, L25
Oskinova, L. M., Hamann, W.-R., Cassinelli, J. P., Brown, J. C., & Todt, H. 2011a, AN, 332, 988
Oskinova, L. M., Todt, H., Ignace, R., et al. 2011b, MNRAS, 416, 1456
Owocki, S. P., Castor, J. I., & Rybicki, G. B. 1988, ApJ, 335, 914
Owocki, S. P., & ud-Doula, A. 2004, ApJ, 600, 1004
Panagia, N., & Felli, M. 1975, A&A, 39, 1
Parkin, E. R., Pittard, J. M., Nazé, Y., & Blomme, R. 2014, A&A, 570, A10
Pittard, J. M., Dougherty, S. M., Coker, R. F., O'Connor, E., & Bolingbroke, N. J. 2006, A&A, 446, 1001
Pittard, J. M., Romero, G. E., & Vila, G. S. 2021, MNRAS, 504, 4204
Puls, J., Markova, N., Scuderi, S., et al. 2006, A&A, 454, 625
Rybicki, G. B., & Lightman, A. P. 1986, Radiative Processes in Astrophysics (Weinheim: Wiley-VCH)
Schmid-Burgk, J. 1982, A&A, 108, 169
Schmutz, W., & Koenigsberger, G. 2019, A&A, 624, L3
Shultz, M. E., Owocki, S. P., ud-Doula, A., et al. 2022, MNRAS, 513, 1429
Silvester, J., Kochukhov, O., & Wade, G. A. 2014, MNRAS, 440, 182
St-Louis, N., Moffat, A. F. J., Ramiaramanantsoa, T., & Lenoir-Craig, G. 2020, in Stars and their Variability Observed from Space, ed. C. Neiner et al. (Vienna: Univ. Vienna), 423
Sundqvist, J. O., Owocki, S. P., & Puls, J. 2018, A&A, 611, A17
Sundqvist, J. O., & Puls, J. 2018, A&A, 619, A59
Trigilio, C., Leto, P., Umana, G., Leone, F., & Buemi, C. S. 2004, A&A, 418, 593
ud-Doula, A., & Nazé, Y. 2016, AdSpR, 58, 680
ud-Doula, A., & Owocki, S. P. 2002, ApJ, 576, 413
Van Loo, S., Runacres, M. C., & Blomme, R. 2004, A&A, 418, 717
Van Loo, S., Runacres, M. C., & Blomme, R. 2005, A&A, 433, 313
Van Loo, S., Runacres, M. C., & Blomme, R. 2006, A&A, 452, 1011
Vink, J. S. 2021, arXiv:2109.08164
Wade, G. A., Neiner, C., Alecian, E., et al. 2016, MNRAS, 456, 2
White, R. L. 1985, ApJ, 289, 698
White, R. L., & Chen, W. 1992, ApJL, 387, L81
White, R. L., & Chen, W. 1994, Ap&SS, 221, 295
Williams, P. M., van der Hucht, K. A., & Spoelstra, T. A. T. 1994, A&A, 291, 805
Woosley, S. E., Heger, A., & Weaver, T. A. 2002, RvMP, 74, 1015
Wright, A. E., & Barlow, M. J. 1975, MNRAS, 170, 41